Biomineralisation: Calcite Structures in Sea Urchin Tests using X-ray Ptychography.

by Gurvinder Singh Chana

Supervised by Professor Ian Robinson

March 2012

Abstract

Biomineralisation is a widespread phenomenon where living organisms produce minerals to strengthen existing tissue. There are two main parts to a biomineralised tissue: the organic part, which makes up about 0.1% of the mass, and the inorganic mineral part, which makes up the rest. However even with such a small percentage of overall mass, the organic part has many implications to the mineral by strengthening it beyond what is capable of the pure crystal. This report is a synthesis on all the research done on biomineralisation of sea urchins. It then goes on to examine the methods of physically examining and imaging the mineralised tissues. Here a method of using coherent X-Ray diffraction simulated by a Fourier transformation is used. Ptychography is one of the iterative algorithm that is simulated in this report to find the feasibility of actually performing the experiment. This is contrasted to Error Reduction and Hybrid Input Output algorithms.

Contents

List of Figures

Chapter 1

Biomineralisation

1.1 Introduction

Biomineralisation is the widespread phenomenon where living organisms produce minerals to strengthen existing tissue, such as shells, teeth and bones. These minerals have a highly ordered atomic structure which lead to specific physical properties such as strength, self repairing properties, and protection. It is because of this, and the fact that biomineralisation is so widespread that it is of much interest to many different scientific fields such as medicine and dentistry, for advancements in understanding bones and teeth, biologists, marine chemists, geochemists and geographers so to understand the role of these minerals, how they are transported and globally cycled, along with how they are used by different organisms. This also crosses over to a specific area in engineering called biomimetics, where biological phenomenon such as biomineralisation are used as a framework for engineering structures. Biominerals are unique in the fact that they are the only part of an organisms that can be held in a fossilised form. From this we know that biomineralisation has been going on for at least 570 million years (Mann (2001)). All of these reasons and more are why biomineralisation is at the forefront of scientific research, and why there is much debate about it.

Due to the complexity of biomineral structures it is necessary to look at all the main aspects of biomineral structures. Firstly we must assess the biological component of these structures, be it the macroscopic organism, or the microscopic structures found at biomineralisation sites. This includes looking at the creation of biominerals by organisms, and how they are repaired, and ultimately used by the organism. Secondly it is necessary to discuss the chemical composition of the biomineral, and any biological component used as it is the biological component that is unique to biominerals. Lastly, we must also look at the physical aspect of the biomineralised tissue, and how much of a part it plays in the structure of organisms. Biominerals have been researched profusely for over a century, however with recent improvements in technology and experimental methods, it is possible to be able to look further into biominerals and and determine their complex ultrastructure.

The structure of biominerals has been evolving over the last 570 million years, fine tuning themselves to function to their maximum ability effectively. These biominerals are much stronger,

MINERAL	FORMULA	ORGANISM	LOCATION	FUNCTION
Calcite	$CaCO_3$	Birds	Eggshells	Protection
Mg-Calcite	$(Mg,Ca)\ CO_3$	Echinoderms	Shells/Spines	Strength/Protection
Aragonite	$CaCO_3$	Fish	Head	Gravity receptor
Vaterite	$CaCO_3$	Gastropod	Shell	Exoskeleton
Amorphous	$CaCO_3.\ nH_20$	Plant	Leaves	Calcium Store

Table 1.1: Calcium Carbonate Biominerals. Adapted from Mann (2001)

and have vastly different properties than just single crystals, and the main reason for this has been their biological involvement, namely the organic aspect of their growth. It is now believed that the organic aspects of biominerals have a large part to play in their structure and growth. However there is obviously much difficulty in finding these structures as we are talking about imaging at the nanoscale. This report will help identify different techniques that can be used in overcoming these problems. However, we cannot just look at the nanoscale, we must also think about the atomic scale, and how the organic parts of the biomineral interfaces, and changes the properties of the mineral interface.

This report will focus mainly on the structure of biominerals at the nanoscale, whilst attempting to provide a broad overview of the current state of research of biominerals. This chapter will focus on the biomineral itself, and the current stage of research. It will explore the structure at all levels, macroscopic, microscopic, nanoscale, and atomic levels. However, because of the wide variety of biominerals it is necessary to choose a specific mineral and a specific organism. There are many different minerals to choose from but the most abundant and common mineral is calcium carbonate. As shown in table 1.1 calcite has three main polymorphs, but the most stable one is calcite. The organism this report will focus on is the sea urchin which is an echinoderm, and the mineral will be magnesium calcite. The reason for choosing sea urchins are because they are in abundance, and are relatively easy to obtain, and prepare for experimentation. They also have been very widely researched and are still an active area of research.

1.2 Sea Urchins

The Echinoidea class of marine animals are found in every ocean, and at every depth. They have many similarities with other marine animals of their phylum, the most obvious is their five fold symmetry which is similar to sea stars and other echinoderms. As you can see in figure 1.1a they are a spherical shape, however they are not always perfect spheres. Some may be oval in shape or even slightly flattened as shown in figure 1.1b, but this makes no difference to their inherent structure. The underside of the sea urchin contain their mouth, usually in the centre, whilst opposite the mouth is the anus. Figure 1.1a also shows the sea urchin to have spines which area called spicules. These are 1-3cm in length, and are there to protect the animal from predators but most importantly for this report, they are made of calcite. The organs of the sea urchin are housed in the test which is a hard shell structure, as shown in figure , and is made of magnesium calcite (Abou and Stone (2011), Jean-Pierre Cuif and Sorauf (2011), Raup (1966), Stephen (2004), Telford (1985)).

(a) Underwater (b) Cleaned Skeletal Shell

Figure 1.1: Sea Urchin

Sea urchins fertilisation occurs when a male sea urchin releases its sperm, and a female releases its eggs into the ocean. Rapid cell division proceeds, and from this stage, they get their bivalve symmetry. Once a spherical shape has been formed, the organism then caves into itself forming a doughnut shape. The two openings form the mouth and the anus. While this is happening, the test is formed by specific cells forming a matrix shape around the forming sea urchin. This is what we call the organic matrix, and is the reason for biomineralisation to occur. This organic matrix which is made of proteins and collagen, is very pliable and resistant to fracture, however in contrast pure minerals such as calcite are very brittle. When these to materials are put together with biomineralisation, they develop into remarkable biominerals with the strength and pliability of both separate constituents, and form a skeletal test around the sea urchin. The following sections will now describe in detail the structure of the test of sea urchins.

1.2.1 Structure of the test

The structure of the test of an adult sea urchin can be split into three distinct sections. The macrostructure, microstructure, and finally the ultrastructure. The macrostructure of the adult sea urchin has already been discussed, but there are a few details with respect to the test that need to be added.

1.2.1.1 Macrostructure

The test is covered by a thin epidermis, and a thicker dermis which is made of nacre, however of more importance is the structure of the aboral surface (top). Figure 1.2a shows a picture of the aboral surface of a cleaned and bleached sea urchin skeletal shell. You can clearly see the five fold symmetry here. The ambulacral areas shown in figure 1.2a contain two rows of tube feet. A close up of this is shown in figure 1.2b. Surrounding the holes, you can see raised circular areas. These are where the spines connect to, and give them their movement, it is rather like a ball and socket joint. In total there are 5 ambulacral areas, and 5 inter-ambulacral areas as shown in figure 1.2a. Each area consists of two rows of mineral, the way these rows are joined together

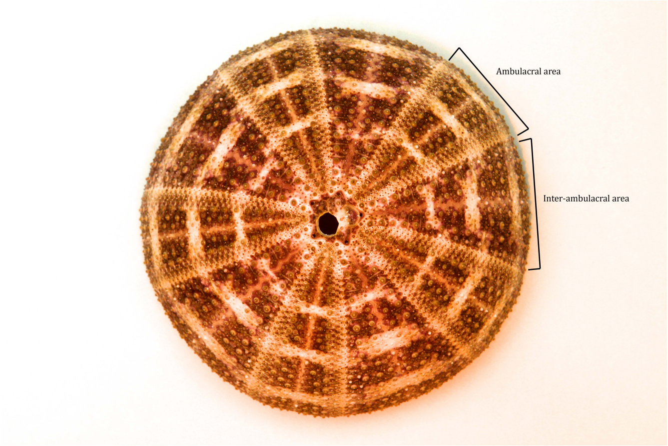

(a) Top view

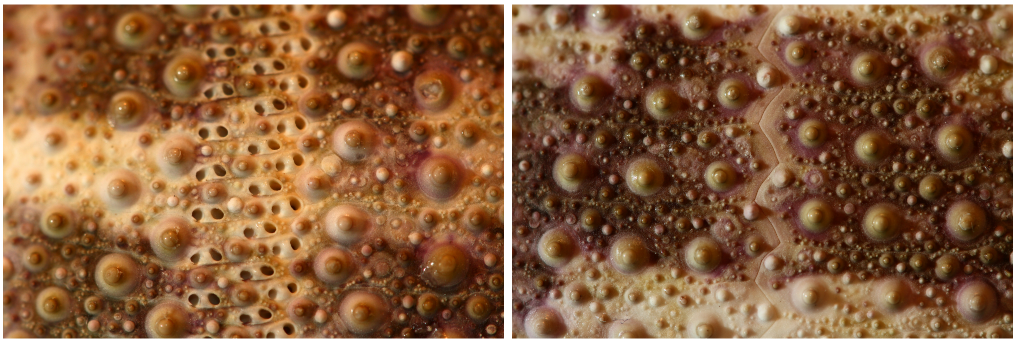

(b) Macro view of tube feet holes

(c) Macro view of connecting plates

Figure 1.2: Cleaned sea urchin photographs

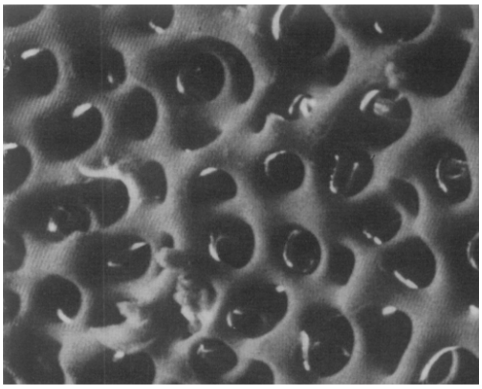

Figure 1.3: porous structure of sea urchin test, adapted from Weber et al. (1969)

can be clearly seen in figure 1.2c. This gives a regular sea urchin 20 rows in total joined together by collagen fibres (Telford (1985)) which are natural proteins that are found in connective tissue. If you look closely at figure 1.2c you can see there are small hexagonal shapes, starting from the join. these are the skeletal plates of which there are hundreds and are also joined by collagen, in a mosaic like fashion (Abou and Stone (2011)).

Described above is the macrostructure of regular adult sea urchins, however as with any evolved species, there are also many irregular echinoderms, some of which have a different number of plates, and are non symmetrical, however the vast majority of adult sea urchins are regular.

1.2.1.2 Microstructure

The sea urchin differs from other biominerals and other animals by employing a fenestrated structure of calcite (Nissen (2012), Weber et al. (1969)), rather that using layers of small crystals. This fenestrated structure means that about 50% of the structure of the mineral is empty space as shown in figure 1.3 (Raup (1966)). This is due to the unique way that they were produced, more details are provided later. The fenestrated structure is called the stereom and can take many different forms. The reasons why echinoderm skeletons can reach a large size is because of this stereom structure, which also gives the structure three main properties. Firstly the structure makes the shell extremely light. The weight of the test in figure 1.1b is 33 grams. Secondly the structure is also very rigid, and finally it is very resistant to fractures.

The form of the stereom is not always the same. Smith (1980) categorised the different forms of the stereom as shown in figure A.1. He also noted, even if one type of stereom was observed on the inner part of a test, it did not mean the same type would be on the outer part. He also noted that there were small differences with the same type of stereom. The most widely observed, and most researched stereom is the labyrinth type. This stereom has also been used for other purposes such as creating a porous gold structure as described by Meldrum (1999) (Meldrum and Seshadri (2000)).

By looking at the diagrams of the stereom and images of it at high magnification, such as 1.3 it is unclear to see where the crystalline nature of the stereom comes from. This is because the curved surfaces appear to be smooth and non planar. There are no indication of faces determined by

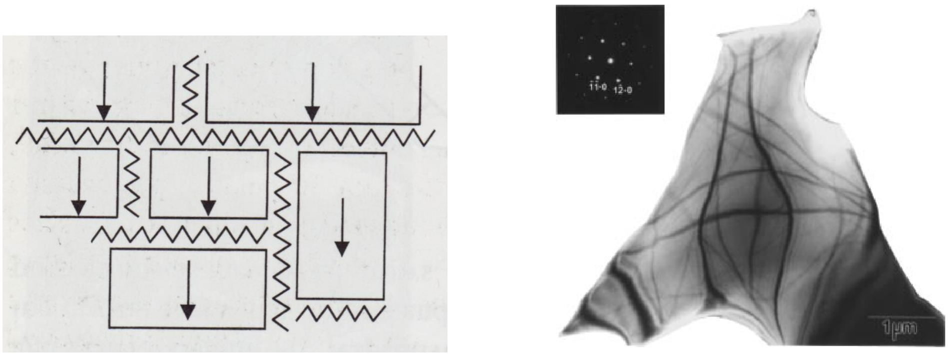

(a) Domain structure in a single crystal of an organic mineral with intercalated organic macromolecules. Adapted from Mann. Mann (2001)

(b) TEM image of a sea urchin spine showing protein matrix. Adapted from Su et al. (2000)

Figure 1.4: The organic matrix

crystal geometry (Nissen (2012)). However it has been shown from x-ray diffraction that they are indeed crystalline, or appear to be crystalline.

The pore sizes are not regular, and differ in different locations. All of the biomineral in the sea urchin contains this fenestrated structure, including the spine and the test. For reference, the average pore size in 1.3 is $28 \pm 16\mu m$.

1.2.1.3 Ultrastructure

There has been much confusion and debate on the ultrastructure of biomineralised calcite over the last century and still their internal ultrastructure is not known despite extensive amounts of research. What is clear, from various diffraction experiments is that the test is diffracts x-rays as a single crystal would(Raup (1966)). The next observation is that there is an internal ultrastructure inside this crystal, what is called the biological component of the sea urchin shell made of various proteins. These two properties of the ultrastructure of the sea urchin shell will now be explored in more detail.

In biomineralisation, the internal organic structure inside of the crystal lattice (not to be confused with the collagen material that joins the individual plates together) is known as the organic matrix (Kenneth Simkiss (1989), Stephen Mann (1989)). This organic matrix within the crystal is best described as a brick an mortar like substance where the brick's are the pieces of calcite while the mortar is the organic matrix. This is pictorially represented in figure 1.4a. As you can see the 'bricks' are not all the same size and the tesselate together in a mosaic like fashion, with a slight gap between each 'brick' for the organic matrix macromolecules.

Although there has been much debate weather this organic matrix exists (Raup (1966), Klein and Currey (1970)), we can clearly conclude that it does indeed exist within the calcite. One of the pieces of evidence for this is the way that biomineralised calcite fractures. Instead of fracturing along the low energy cleavage planes as one would expect, similar to synthetic calcite, it fractures more like a glass. These and other mechanical properties which will be discussed in the next section give us irrefutable evidence of the organic matrix(Mann (2001), Kenneth Simkiss (1989)).

This organic matrix takes up to 1% of the space in the test, and 0.01% of the weight (Mann (2001)). The makeup of the organic matrix has been difficult to determine, but with modern techniques it has been realised that protein is a major constituent in its makeup(Kenneth Simkiss (1989)). Recent research have identified 110 different proteins as a component of the sea urchin test organic matrix. A full list of these proteins can be accessed on the internet via Mann's 2008 paper (Mann et al. (2008)).

Another area of much controversy has been the nature of the crystal parts of the test. The nature of this debate has been weather the crystal is indeed a single crystal, or a composite of many crystals or polycrystalline. The arguments for a single crystal come from diffraction experiments, and experiments under polarised light which clearly show the single crystal form of the lattice. This single crystal is visible in the test and the spine of the sea urchin however other parts of the calcite, such as the lantern, do not show this regularity. It has been argued that the crystal is made up of millions of tiny crystallites that are all aligned perfectly with respect to the c-axis and the a-axis so that they appeared to be a single crystal under diffraction experiments (Kenneth Simkiss (1989), Raup (1966), Donnay and Pawson (2012), Towe (2012), Arbor and Engineering (1984)).

Although the exact ultrastructure of the test is under much controversy and unknown, we can so far conclude that there is indeed an organic matrix inside of the fenestrated calcite structure of the test. The calcite could either be made of a single crystal, or a mosaic of many crystallites that are all orientated in the same direction. The organic matrix is made of two parts, insoluble, and soluble matrix. Much of its constituent parts are proteins. The role of the organic matrix will be discussed further.

With new technology, we are able to probe the resolutions required to view the matrix structure. This is shown in figure 1.4b where you can clearly see the voids where the protein matrix resides. The diameter of these voids, or the 'mortar' is about $80nm$. Note that the organic matrix does not have any regularity like the underlying crystal, and that there is also a wide range of matrix diameters.

1.2.2 Function of the Test

The test has many functions, primarily it is there to protect the organs of the sea urchin. It is also provides a place for the spine of the sea urchin to attach onto. They are attached via a ball and socket type joint which allow them to move slightly. However we are most interested in this protection aspect of the test, and how it has evolved and adapted after millions of years.

We can categorise the test into having three main properties; strength, lightweight, resistance to stress. As explained earlier, the strength of the test comes from the dome shape of it, thus to a first approximation the stresses will be dissipated as in a dome on a building. The tensile forces in the test will attempt to increase the dome's diameter, but this will be held together with the structure Tsrpunsry and Busncr (1993).

The lightweight property of the test comes from its fenestrated structure and that 50% of the volume of the test is occupied by the pores. Compared to synthetic calcite, this effectively halves the weight of the test. This, accompanied with the fact that the test is dome shaped means that it has a low centre of gravity. It could be thought that because of the fenestrate structure and the single crystals of calcite that the structure of the test be relatively weak, but again due to the remarkable inclusion of the biological organic aspect it is far stronger than expected. It is in fact many times stronger than calcareous rocks and mollusk shells (Weber et al. (1969)).

The resistance to stress is one of the main aspects of the test and what is most remarkable about it. Normal calcite is extremely brittle and easy to stress and strain, however the strength to weight ratio of biomineralised calcite in sea urchins is much higher than any other type of calcite (Weber et al. (1969), Weiner (1986)). One of the reasons for this is the collagen protein that is used to bond individual plates together. This collagen allows the whole test to flex internally while retaining its rigid structure, however this is yet to be qualitatively proven. Another reason is due to the fenestrate structure, and the fact that any cracks would not be permitted to grow beyond the next pore. So any cracks that do form, no not go further than $80\mu m$.

1.2.3 Biomineralisation of the Test

Although this report is not on the mechanism of biomineralisation, is is prudent to say a few things about it. The organic matrix is what allows the biomineralisation to occur. It provides many functions that allow this process to occur. Firstly it contains the initial nucleation sites for the calcite to grow around. In the provides further by feeding the crystal, allowing it to grow. It is then also able to inhibit growth of the crystal. The organic matrix is thus very important to biomineralisation.

The calcium part of the calcite is sourced from the seawater around the sea urchin while the carbonate is derived from the bicarbonate in the water. These are then deposited by the organic mineral allowing the crystal to grow and for its structure. For more information about the process of biomineralisation, please see Stephen Mann (1989).

1.3 Imaging Techniques

With conventional optical microscopy at the visible light wavelength we are limited in resolution to $200nm$ due to diffraction. With our organic matrix being $80nm$ in diameter, this is clearly not enough resolution. However we can clearly image the pores of the fenestrate structure, but to go further we must use other means.

Electron microscopes are the next logical choice as they could potentially probe up to $50pm$. There are two types of electron microscopes that are widely used today. The first is the transmission electron microscope, which accelerates electrons toward a sample through an objective lens. This then scatters the electron providing it with information about the structure of the sample. This is the highest resolution imaging that can be realistically used, and an example of this is the organic matrix structure in figure 1.4b.

The biggest problem with TEM is sample preparation. The sample must be extremely thin, a few hundred nanometers at the maximum. This obviously represents a problem with the scope and range of TEM. Scanning electron microscopes are the other option, and they do not require a thin sample, however you there are still many issues with sample preparation. There are other imaging techniques that have been used to image biominerals such as atomic force microscopy, however these are of limited use in biomineral imaging.

One option that remains are to use x-rays to image. Their resolution is between that of traditional optical microscopes, and electron microscopes at about $0.1nm$. This resolution is more than enough to image the organic matrix within biomineral calcite. It also has a much deeper penetration depth, allowing for less stringent sample preparation. The rest of this report will show how x-rays can be used to image sea urchins.

1.4 Importance of Sea Urchin Tests

Important lessons can be learnt from sea urchin tests. Biomimetic engineering concerns mimicking biological examples using synthetic materials to create new products. As you can see this would be particularly useful with biominerals, especially with the strength of sea urchin tests. A different type of stronger concrete could be designed, as well as improving dome structures, and even bridges. We have yet to learn from the sea urchin example.

The sea urchin is one of the most widely studied biomineral examples mainly because of its abundance. However as biomineralisation is such a widespread phenomenon, the lessons learnt from the sea urchin tests could be applied to other biominerals. This could have profound implications in dentistry, and biomedical sciences. This is why imaging the sea urchin is an important task.

Chapter 2

X-Ray Diffraction

2.1 Diffraction Theory

As we have seen, the test of the sea urchin appears to be a single crystal with sharp Bragg peaks when imaged using x-ray diffraction. Although there are many other imaging techniques, we can use the advantage of the crystalline nature of the calcite to reconstruct the sample from diffraction patterns achieved using x-ray diffraction. The main advantage of using x-rays would be the high resolution images that could be achieved. The wavelength of a soft x-rays are $10nm - 0.10nm$ while hard x-ray, which have higher penetrating depth due to their higher energy have typical wavelengths of $0.10nm - 0.01nm$. The greater penetration depth of hard x-rays also mean that the sample does not have to be too thin. The sample could also be live, rather than dehydrated, and stripped off its organic material. The only potential problem with hard x-rays are that the higher energy could potentially destroy the sample, however with the energies that we are currently using and by limiting the exposure to the sample, this could be limited. It would be quite apparent if a sample was to start to distort in a diffraction experiment. The technique of using x-ray diffraction to probe crystals is called crystallography.

X-rays diffract off the planes in a lattice structure. These planes are similar in magnitude to the x-ray wavelength, therefore can be probed by them. Incoming x-rays are scattered by successive planes in the lattice, as shown in figure 2.1. The scattered waves then interact constructively and destructively, and at a focal plane, they produce a diffraction image of constructive and destructive interference. These can then be measured using a detector. The reason for the scattering is given by the difference in path length's at specific angles. When the phases are equal at specific angles, we will have constructive interference. This is governed by the Bragg condition which is shown in equation 2.1

$$2dsin\theta = n\lambda \tag{2.1}$$

Where d is the distance between the lattice planes, and where λ is the wavelength of the incoming wave. n is just an integer that corresponds to a 2π shift in phase. There are a few requirements for the Bragg condition to hold true, the most important of these being the crystal must be sufficiently large. This clearly represents a problem to us when using x-rays to probe finite sized

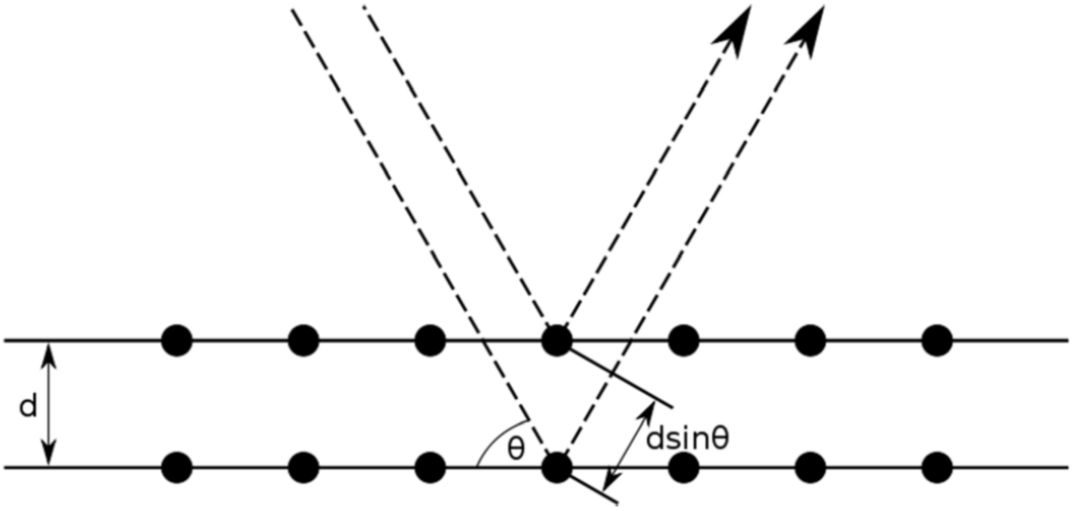

Figure 2.1: Bragg Diffraction. Adapted from http://en.wikipedia.org/wiki/Bragg_condition accessed on 28/03/12

crystals, however the chunks of crystals are still large enough ($\sim 1\mu m$) when compared with the x-ray wavelength.

Figure 2.1 shows the case of a simple crystal undergoing Bragg diffraction, however this is identical to larger and more complicated crystals, the diffraction patterns will start to become more complicated with lower resolution. We will also be using coherent x-rays to probe the sample. Coherent diffraction will allow to remove the need for lens's that are used to focus incoming beams of x-rays. Lensless diffraction allows us to remove the problems associated with lens's such as aberrations, which will allow us to have a higher resolution, however without utilising a lens, we encounter a phase problem which will be discussed further. We will use the term CXD to define coherent x-ray diffraction. Before we continue, we must realise that we need a full mathematical description of how coherent diffraction occurs.

2.2 Fourier Transform

The Bragg equation2.1 is used to measure inverse distances in reciprocal space. Reciprocal space is used to help us define a crystal lattice. To move into reciprocal space we use what is called a Fourier transform. The lattice planes are defined by the usual h, k, l values. We can then define the real lattice vectors as

$$\mathbf{R}_n = n_1\mathbf{a} + n_2\mathbf{b} + n_3\mathbf{c}$$

Where n_i's are any integer. The reciprocal lattice vector is then defined as.

$$\mathbf{G}_n = h\mathbf{a}^* + k\mathbf{b}^* + l\mathbf{c}^*$$

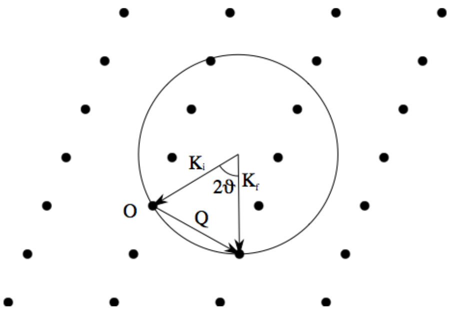

Figure 2.2: Ewald sphere

Max von Laue developed three equations for diffraction to occur. There are;

$$\mathbf{a} \cdot \nabla Q = 2\pi h$$

$$\mathbf{b} \cdot \nabla Q = 2\pi k$$

$$\mathbf{c} \cdot \nabla Q = 2\pi l$$

Where Q is the scattering vector shown in figure 2.2 between the incident and scattered wavevector $\mathbf{k}, \mathbf{k}'$. The figure is called an Ewald sphere, which is in reciprocal space. The distance between the points which are Bragg peaks are inverse distance. The Laue condition then states that for scattering, $\mathbf{Q} = \mathbf{G_n}$. This then reduces to the Bragg condition, showing how the Bragg condition can be used in coherent diffraction.

$$|\mathbf{Q}| = \frac{4\pi \sin\theta}{\lambda} = |\mathbf{G}_n| = \frac{2\pi}{d_{hkl}}$$

$$\therefore \lambda = 2d \sin\theta$$

As explained, a Fourier transform takes us from real space into reciprocal space as below.

$$A(\vec{q}) = \iiint_{-\infty}^{\infty} \rho(\vec{r}) e^{-i\vec{q}\cdot\vec{r}} d^3\vec{r} \rightarrow \mathcal{F} \tag{2.2}$$

Where $A(\vec{q})$ is the scattering amplitude, and $\rho(\vec{r})$ is the density of the sample. Once we are in reciprocal space, we can return to real space by using an inverse Fourier transform.

$$\rho(\vec{r}) = \iiint_{-\infty}^{\infty} A(\vec{q}) e^{iq\cdot\vec{r}} d^3 r \vec{=}\longrightarrow \mathcal{F}^{-1} \tag{2.3}$$

2.2.1 DFT and FFT

Computationally, we must use a discrete version of the Fourier transform. This is defined by the equation below.

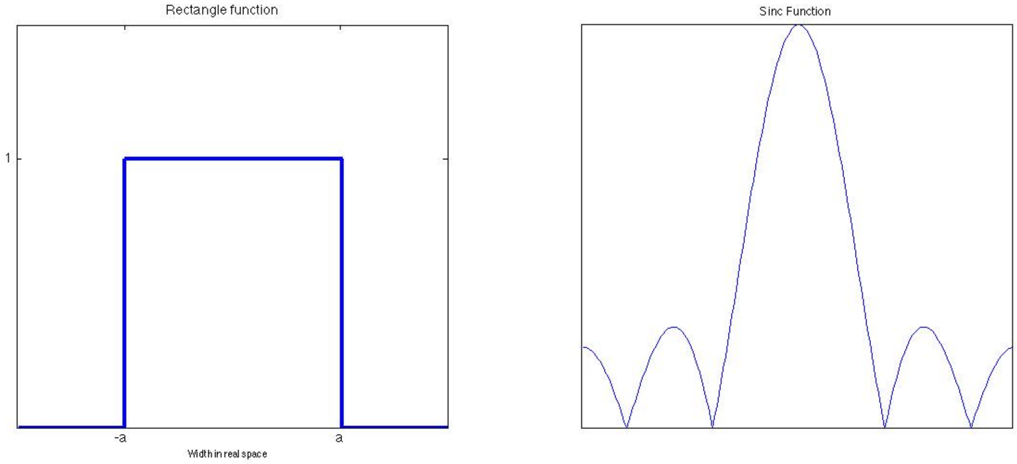

(a) Rectangular step function (b) Sinc function obtained after FFT

Figure 2.3: FFT example

$$A_j = \sum_{n=0}^{N-1} \rho_n \cdot e^{-i2\pi \frac{j}{N} n} = \mathcal{F} \tag{2.4}$$

Where N is the array size, for computation reasons this is usually a power of 2. The inverse of the DFT is then.

$$\rho_n = \frac{1}{N} \sum_{j=0}^{N-1} A_j \cdot e^{i2\pi \frac{j}{N} n} \tag{2.5}$$

When we move from a continuous function to a discrete one, we encounter an aliasing problem, which is where two samples are indistinguishable from each other. If this occurs then we are unable to reconstruct the sample image. To circumvent the problem we must apply the Nyquist-Shannon sampling theorem. The theorem states that the spacing of the digital sample must be at least twice the highest sampled frequency.

The computer program that will be used for the processing is called Matlab. Matlab is a numerical computing environment and employs a version of the DFT called the fast Fourier transform (fft). A 1d example of the FFT is shown in figure 2.3. The code for this is given in B.1.

The expected Fourier transform can be calculated from equation 2.2 as follows.

$$\int_{-a}^{a} \rho(x) e^{2\pi i k \cdot \vec{r}} = \int_{-a}^{a} 1 \cdot e^{ik \cdot x} dx = \left[\frac{e^{ik} \cdot x}{ikx} \right]_{-a}^{a} = \frac{\sin kx}{kx} = sinc \tag{2.6}$$

As you can see, this is for a simple example in 1d, however with the fft in Matlab, this can be used in any number of dimensions. Now we have our amplitude information in reciprocal space, it is just a matter of doing the inverse fft. This then takes us back to real space, and thus our image.

2.3 The Phase Problem

As described in the previous section, the FFT can be reversed using the inverse FFT function in Matlab. This is simple and takes us right back to our original sample. However in reality, this is not the case. The first thing to not is that the amplitude is not what is measured at an experiment, we measure intensity. These are linked by the following equation where $A(Q)$ is the amplitude, while $I(Q)$ is the intensity.

$$I(Q) = |A(Q)|^2 \tag{2.7}$$

To explain the consequences of this we must look at our scattering amplitude, which is according to the convolution theorem.

$$A(Q) = \sum e^{\iota \mathbf{GR}} \sum f_j(Q) e^{i\mathbf{Q}\cdot\mathbf{R}} \tag{2.8}$$

$$|A(Q)|^2 = \sum e^{iQ(\mathbf{r}_j - \mathbf{r}'_{\mathbf{j}})} \tag{2.9}$$

As you can see, the only information we end up with relates $\mathbf{r}_j$ to $\mathbf{r}'_j$. All the information relating $\mathbf{r}_j$ to the origin is lost, this is essentially all the complex phase information. We can logically realise this by understanding that our detectors can only measure amplitude, and the are not able to capture any complex phase's. We can also confirm this by analysing equation 2.2. This is what is called the phase problem. Without any of the phase information, we are unable to accurately reverse the diffraction pattern in Matlab to reproduce the sample. This is why x-ray diffraction imaging is not as simple as it may see.

2.4 Phase Reconstruction Techniques

With the advent of computer technology, there are many algorithms that we can employ to help us reconstruct our phase information. These algorithms have been developed using iterative procedures that are very computer intensive, however they are very effective at recovering the phase information lost when performing x-ray diffraction information. There are three algorithms that will be discussed and used in this report, and in the simulations.

2.4.1 Error Reduction

The first Algorithm is called Error Reduction (ER) which was developed by J.R. Fienup in 1978Fienup (1978). The steps involved are outlined below. Our real amplitude will be $F(x)$.

1. Guess the sample. For the simulation a square shape was assumed.
    - $g_n(x)$
2. Take the sample into reciprocal space using FFT.

- $\mathcal{F}[g_n(x)] = G(x) = |G(x)|e^{i\psi(g)}$

3. Replace the amplitude of the sample with the square root of the intensity of your measured data. keeping the phase information.
    - $G'(x) = |F(x)|e^{i\psi(g)}$
4. Take everything back into real space using inverse FFT to create a new guess.
    - $\mathcal{F}^{-1}[G'(x)] = g'(x)$
5. Set everything outside of the original guess to zero on this new guess.
    - $g_{n+1}(x) = \begin{cases} g'(x) & x \neq \gamma \\ 0 & x = \gamma \end{cases}$ where γ is the area outside the support
6. Repeat until desired iterations.

To monitor the progress of the algorithm, and to compute the error, we use the sum squared error according to equation 2.10. When the error plateaus, the algorithm has essentially converged upon a solution, correct or not.

$$\frac{\sum[|G(x)| - |F(x)|]^2}{\sum |F(x)|^2} \tag{2.10}$$

Example of ER

The first step was to create a sample. This was a 2d square with side length 56 pixels in an array with length 300 pixels as shown in figure2.4a. This is the sample we are trying to recover. The diffraction pattern for this square was then obtained, as shown in figure 2.4b. This diffraction pattern would be our measured intensity, and from this, we would need to recreate the phase information to get back to our sample.

Then a guessed figure was created, slightly bigger than the sample, this is shown in figure 2.4c. After using the algorithm many times, it was found that if the guessed image was too large, or too dissimilar to the actual image, the algorithm would converge upon the wrong solution, while still giving a small error. After 1000 iteration of the algorithm, the recovered image is showed in figure 2.5b. This recovered image as you can see is smaller than the guess that was started with, and is the same size as the original sample. On this occasion you can clearly see that the algorithm successfully managed to recover the original image. The error in this was lower than 10^{-6}using the SSE formula in equation 2.10.

For reference purposes, the phase information is also shown in figure 2.4e. If we look back at the recovered image 2.5b, we can see a small amount of ghosting. Even though the error is sufficiently small, you can still see some artefact in the image that shouldn't be there. This is already showing the shortcomings of this algorithm. The code that provides the function of the algorithm is produced in B.2.

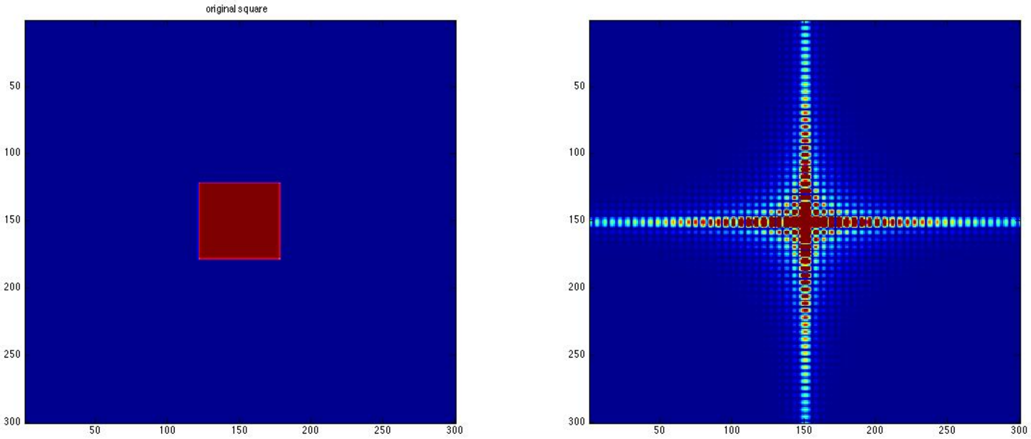

(a) Square Sample

(b) Diffraction pattern from square

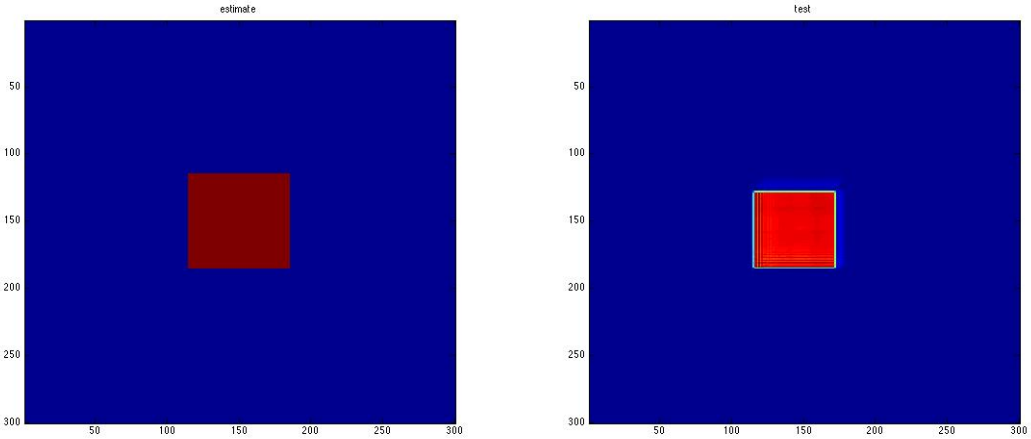

(c) Guessed sample size

(d) Recovered image

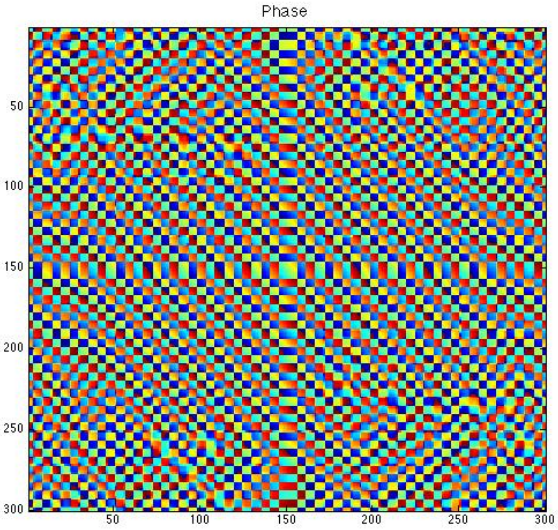

(e) Phase information that was recovered

Figure 2.4: ER example using simple square

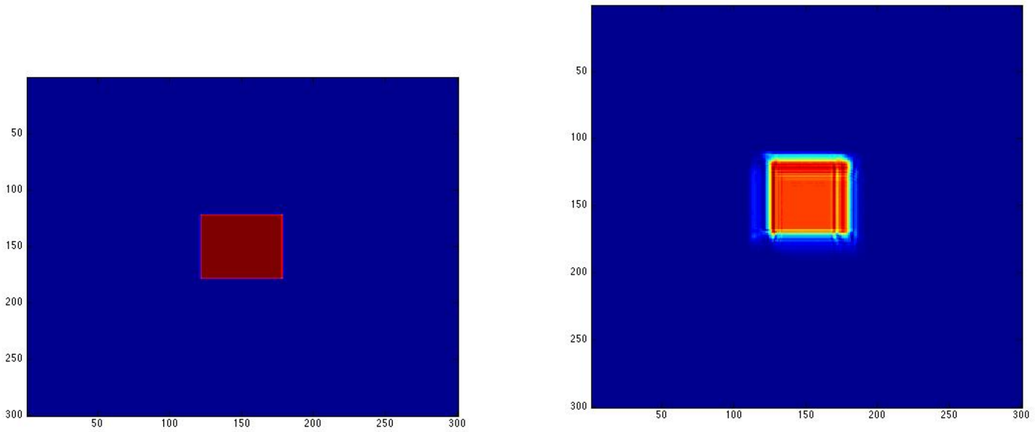

(a) Original sample

(b) Recovered image

Figure 2.5: HIO Example

2.4.2 Hybrid Input-Output

Hybrid input output (HIO) is almost identical to ER but for the last step, number 5. Instead of discarding the area outside of the support, it used used to generate the new guess according to the strength parameter β.

$$g_{n+1}(x) = \begin{cases} g'(x) & x \neq \gamma \\ g'(x) - \beta g_n'(x) & x = \gamma \end{cases}$$

The β parameter usually is set to 1, but can be reduced to reduce the strength of the feedback loop.

After the HIO and ER algorithms were introduced by Fienup, the problem of uniqueness of the solution arose. In the 1D case, there are no unique solutions, so without the phase information, it cannot be reconstructed. However with 2D and higher dimensions, a unique solution can be found provided that the diffraction pattern is oversampled by a factor of 2. This was found by Bates (1984).

HIO Example

With this example, the guessed sample was significantly bigger than the original sample shown in figure 2.10a, however you can still see that the algorithm managed to converge onto a solution that is quite close to the original sample. Another limitation in this example is that it was only run for 300 iterations, however the error remained small (10^{-3}).The function to perform the HIO code is given in B.3.

As you can see, the reconstructed image has more artefacts than the error reduction algorithm, however if performed with identical variables, than the HIO usually responds quicker and more positively each iteration.

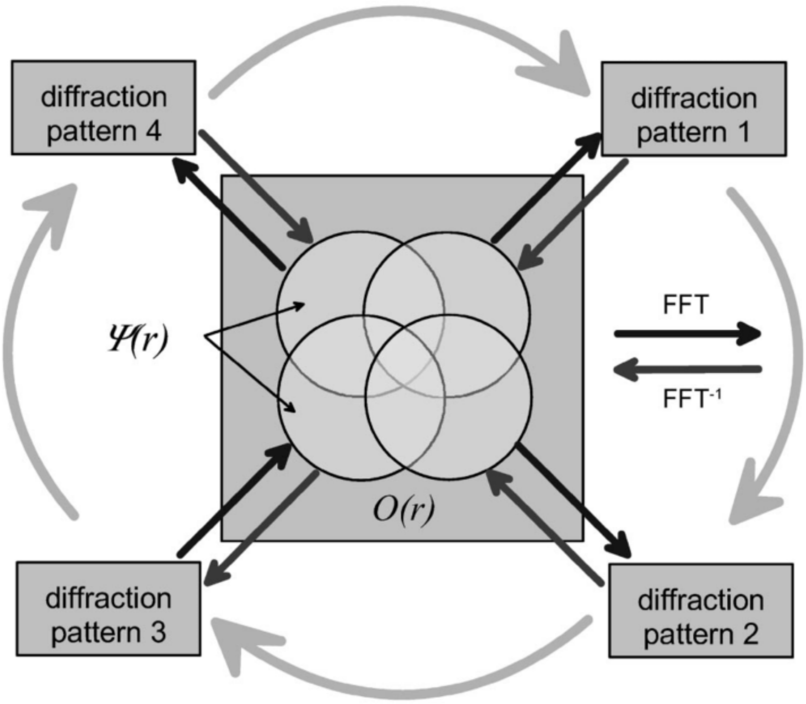

Figure 2.6: Representation of Ptychography, adapted from Rodenburg et al. (2007a)

2.4.3 Ptychography

Ptychography is the final algorithm to be looked at, and is fundamentally different from ER and HIO. It was developed by Walter Hoppe in 1969 Rodenburg et al. (2007a). Ptychography works by using multiple overlapping diffraction patterns to help solve for the phase information required for image reconstruction. It is similar in technique to HIO and ER but because it uses multiple diffraction patterns with an overlapping region that helps solve for the image. Figure 2.6 shows the circular probes that overlap each other, and how each diffraction pattern is used to reconstruct the image. Each arrow can be counted as an iteration, however if we count the entire loop as an iteration it is more difficult to compare with the ER and HIO algorithms.

The steps involved in solving for the phases using are following Rodenburg's conventions, and are outlined here. R represents the probe position. $O_{g,n}(\mathbf{r})$ is our initial guessed object. $\Psi(\mathbf{k},\mathbf{R})$ is the diffraction pattern from probe position Maiden and Rodenburg (2009), Rodenburg et al. (2007b).

1. Calculate the guessed diffracted wave at a probe position R by multiplying current (or initial) guess with the probe at position R .
    - $\psi_{g,n}(\mathbf{r},\mathbf{R}) = O_{g,n}(\mathbf{r}-\mathbf{R})$
2. Take the function into reciprocal space using FFT.
    - $\mathcal{F}[\psi_{g,n}(\mathbf{r},\mathbf{R})] = \Psi_{g,n}(\mathbf{k},\mathbf{R}) = |\Psi_{g,n}(\mathbf{k},\mathbf{R})|e^{i\theta_{g,n}(\mathbf{k},\mathbf{r})}$

3. Replace the guessed amplitude with the known amplitude from diffraction experiment.
    - $|\Psi_{g,n}(\mathbf{k},\mathbf{R})|e^{i\theta_{g,n}(\mathbf{k},\mathbf{r})} \longrightarrow |\Psi(\mathbf{k},\mathbf{R})|e^{i\theta_{g,n}(\mathbf{k},\mathbf{r})} = \Psi_{c,n}(\mathbf{k},\mathbf{R})$
4. Take the corrected wave back into real space.
    - $\mathcal{F}^{-1}[\Psi_{c,n}(\mathbf{k},\mathbf{R})] = \psi_{c,n}(\mathbf{r},\mathbf{R})$
5. Update the guessed object at probe position R using the update function.
    - $O_{g,n+1}(\mathbf{r}) = O_{g,n}(\mathbf{r}) + \frac{|P(\mathbf{r}-\mathbf{R})|}{|P_{max}(\mathbf{r}-\mathbf{R})|}\frac{P^*(\mathbf{r}-\mathbf{R})}{|P(\mathbf{r}-\mathbf{R})|^2+\alpha}\beta(\psi_{c,n}(\mathbf{r},\mathbf{R}) - \psi_{g,n}(\mathbf{r},\mathbf{R}))$
        - The β parameter controls the strength of the update procedure.
6. Move onto the next overlapping probe position. Continue steps until error is small.

The error can be computed in the same way as HIO and ER with a slightly modified version of the SSE shown in equation 2.11.

$$\frac{\sum[|\Psi(\mathbf{k},\mathbf{R})|^2 - |\Psi_{g,n}(\mathbf{k},\mathbf{R})|^2]^2}{\sum|\Psi(\mathbf{k},\mathbf{R})|^2} \tag{2.11}$$

The overlap parameter is the most important variable in this algorithm. The code in B.5 clearly shows the variable overlap parameter. If the overlap is set to zero, then the algorithm essentially computes the code similar to HIO. An overlap of 50% yielded the best results, and is recommended for ptychography simulations.

Ptychography example

In this example. an image was used rather than a square, as it would have been readily reproduced, and an image would really show the strength of the algorithm. The code is quite laborious and is shown in B.5, with the top hat function to create the probe shown in B.4. The reason why the probe is circular is because that is the most likely shape of the illumination beam if performed experimentally.

The images in figure 2.7 show the algorithm at work for a simple brick and mortar like picture. This is similar to what we would actually find in biomineral calcite. Here you can see how quickly the error drops off to effectively zero. 100 iterations are about enough for this algorithm to converge on the right solution. And if we take into account that there are 25 different probe positions in this image, we can quickly realise that the solution was converged upon in 4 loops of the image reconstruction phase.

The original sample is coloured in red and blue, as with the images in ER and HIO representations on Matlab. This is because Matlab colours in a zero value with blue, and a one value with red. The reconstructed image is not exactly the same colour as the original sample, but it is very close, as you can see by the error, however because it is not exactly the same value, Matlab changes the shade of colour so you can distinguish between the two.

This leads on to the next example. Figure 2.8 shows what would happen if you inverse the image, so that the crystal are contained in the small sections of red mortar, and have large blue voids.

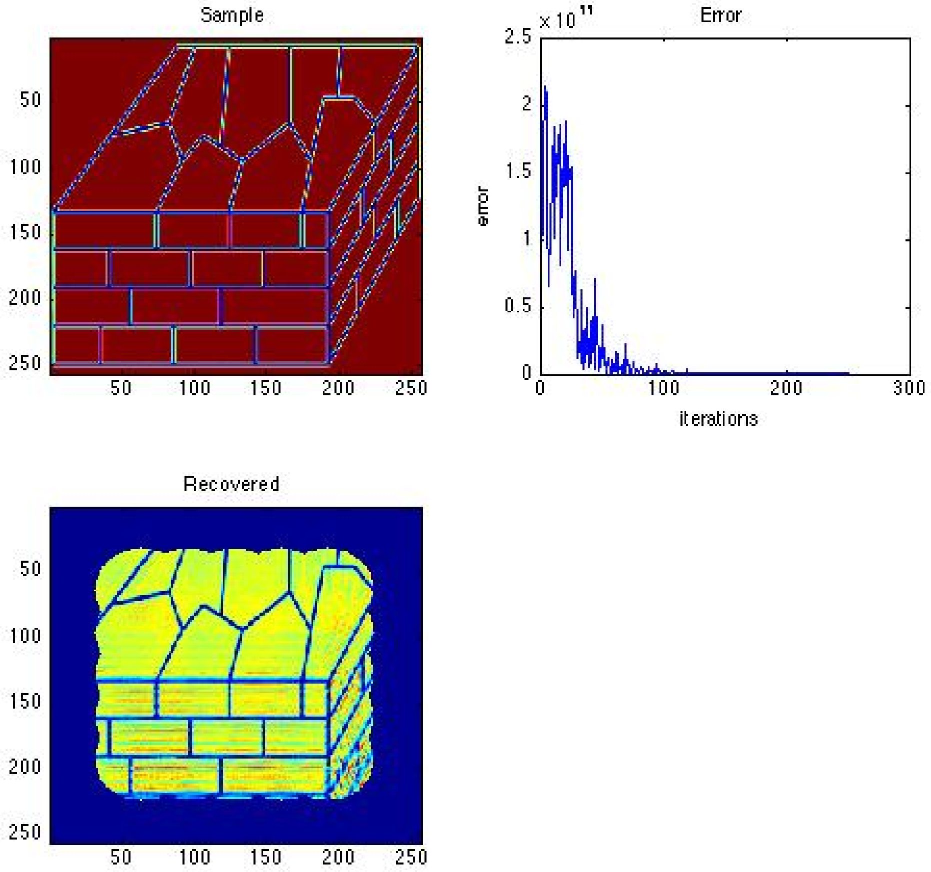

Figure 2.7: Ptychography algorithm reconstructing brick and mortar pattern

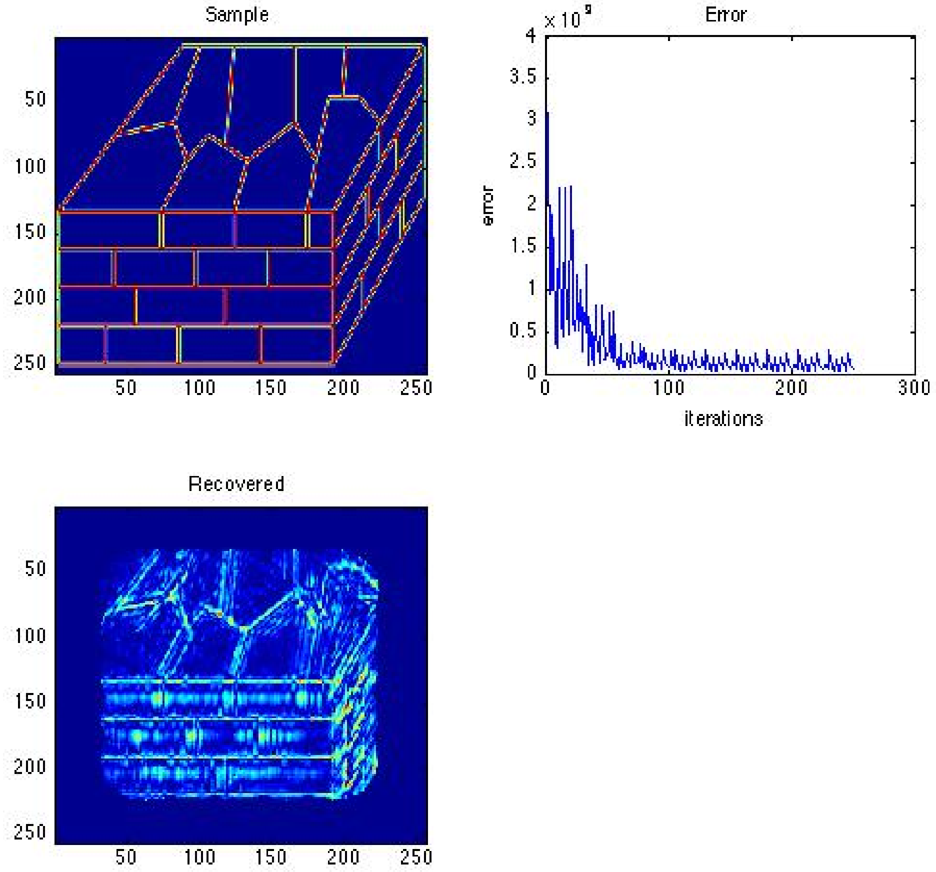

Figure 2.8: Ptychography algorithm reconstructing inverse brick and mortar pattern

This is a classic case of finite crystal sizes, and the under sampling problem that was discussed. Here you can see that the reconstructed image remains fuzzy and slightly blurred. For reference, the other two algorithms could not converge upon a solution, however, even though the error is still large, you can just about make our the correct solution in the representation. This shows the strengths of the Ptychography, but also shows that it still succumbs to the theoretical limits of x-ray diffraction.

2.5 Simulations

Now having been through the background, and the theory of biomineralised calcite, and coherent x-ray diffraction, we can now look at some of the results of the simulations that were run during the project. The first few sets of simulations are from ER and HIO algorithms, but before these are shown, a brief discussion of the experience of using ER and HIO is necessary.

It was found that ER would readily converge onto a solution of a square sample accurately and quickly if the guessed sample was not too much bigger than the actual sample. A limitation of the code is that if your guess is smaller than your sample, the solution to the algorithm is somewhat evasive because of equation in step 5 of the ER code. This step involves setting everything outside of the guess to zero. This prevents the algorithm converging on a solution that is larger than the guess.

Another limitation of ER is that once defects are placed upon the crystal, for example a line taken out of the structure, it would have more difficulty in finding the right solution, and most of the time it would converge upon the wrong solution. This case can be clearly recognised when the error is low, and the solution is not correct. If the voids, or dislocations within the sample were sufficiently large, then the algorithm would get closer to finding the correct solution.

HIO was significantly clearer in attempting to reconstruct the images, however it still suffered from the same problems of ER. It would occasionally hunt around for a solution, rather like a camera lens would hunt around for a focus point, and then would proceed to converge upon the wrong solution, like a camera lens would focus at the wrong place. This is the main problem with both of these algorithms, they are somewhat unreliable. This can be explained by the uni

One solution to prevent the algorithm from converging upon the incorrect solution was to use both of the algorithms together successively. This was done and the resulting code reproduced in B.6. With this code, we were able to clearly see which situations the code was able to converge upon solutions. For example, figure 2.9 shows the algorithm attempting to converge upon a solution. In this example the support is slightly larger than the sample, however the defect in the sample is only 5 pixels wide. This brings up the problem with the algorithm, as you can see it fails to converge upon a solution. However if we contrast this to if the support was the same size, the algorithm would converge to the correct solution. So it is important for the ER and HIO to get the support size to be correct. This is in total contrast to ptychography which allows for any kind of support size, even none.

As you can see so far, the sample images that have been used are squares with single voids running through them. This would represent the voids for the organic matrix. However to construct a more realistic view of biomineralised calcite, we need to create a brick and mortar like structure as done with the ptychography example in figure 2.7. This would indeed show us if ptychography would be able to probe the complex nature of the biomineralised calcite. The first example is a perforate structure, with a regular periodic matrix void. This has smooth edges and has been overlaid with some random noise to represent variations in the crystal. Figure 2.10a shows this sample, along with figure 2.10b which shows the reconstructed image using HIOER algorithms, and figure 2.10c which shows the image being reconstructed using ptychography. The ERHIO algorithms have the same size support as the sample, so they make a good attempt at converging upon the solution, however you can clearly see the merits of ptychography in resolution. The ERHIO still looks slightly blurred and does not have the detail that the Ptychography has.

One of the main points to not about this simulation is that it took a few attempts to find the optimum setting for ERHIO and indeed ptychography. For ERHIO, the size of the sample that and the guess was made the same, this was essential for the convergence of the image. It was also necessary to choose the correct size probe, too small would not yield any results, while too large a probe would converge on the wrong solution. With the Ptychography, it was essential to get the overlap parameter right. The same overlap parameter cannot be used in every image, as each image is different, and requires a different parameter. The periodic nature of the lattice that was being sampled meant that if the distance between the probes was the same as the lattice

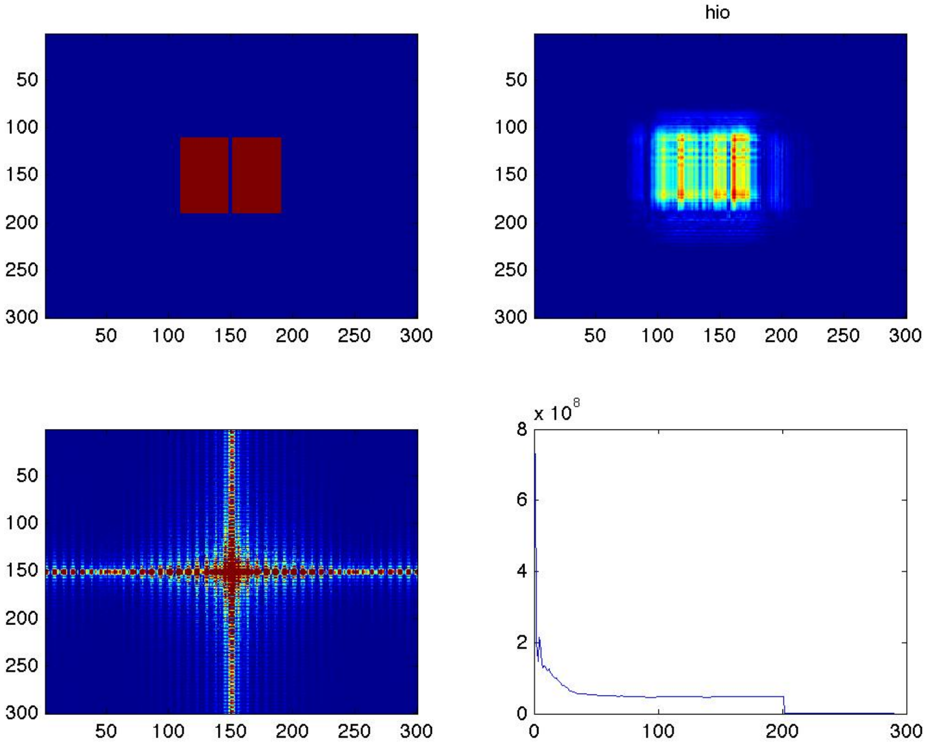

Figure 2.9: ERHIO code at work

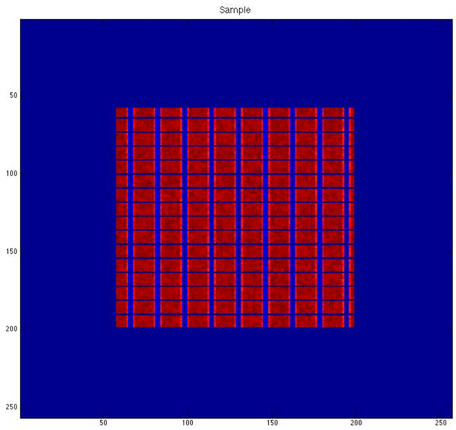

(a) Original sample

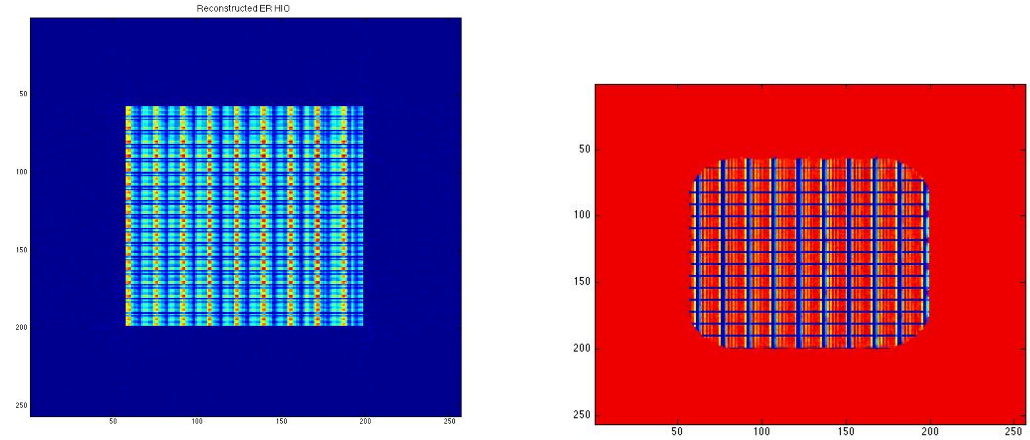

(b) ERHIO reconstruction with optimised settings

(c) Ptychography reconstruction

Figure 2.10: Calcite simulation results

periodicity, then it would not converge upon a solution. To solve this the overlap parameter was adjusted so that the algorithm would converge, and as you can see the algorithm has managed to recover every detail in its scope.

Because of the unknown nature of the voids in the organic matrix in the test of the sea urchin, it was necessary to have a non periodic lattice. Figure 1.4b shows the organic matrix in the spine of a sea urchin which could potentially be very similar to the structure of the test. This image was imported into Adobe Photoshop, and adjusted so it could be used in Matlab. It was cleaned up, and adjusted to give high contrast. It was then converted into 8bit greyscale and imported into Matlab. This image was then reconstructed using the two algorithms and the results are shown in figure 2.11.

In 2.11a you can clearly see that the algorithm has rotated the image by 180degrees. It has also attempted to converge upon a solution, however you can clearly see the fuzziness of the image that is characteristic of aliasing problems. There problems are entirely absent in the recovered ptychography image as shown in 2.11. The voids that contain the organic matrix are

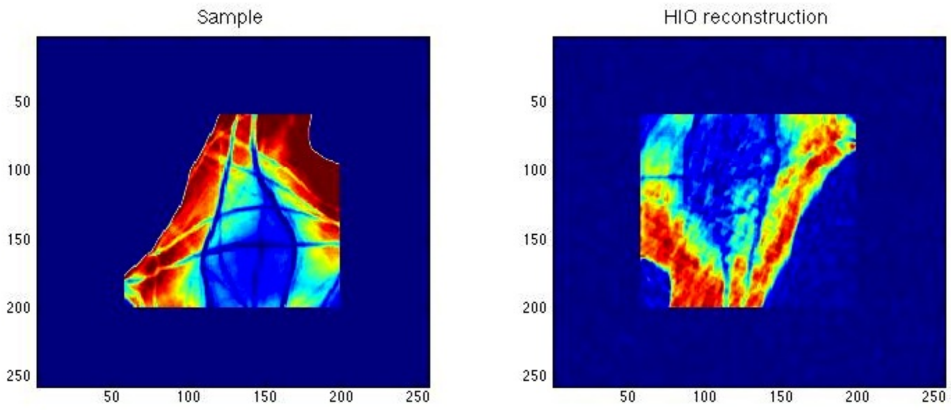

(a) ERHIO reconstruction

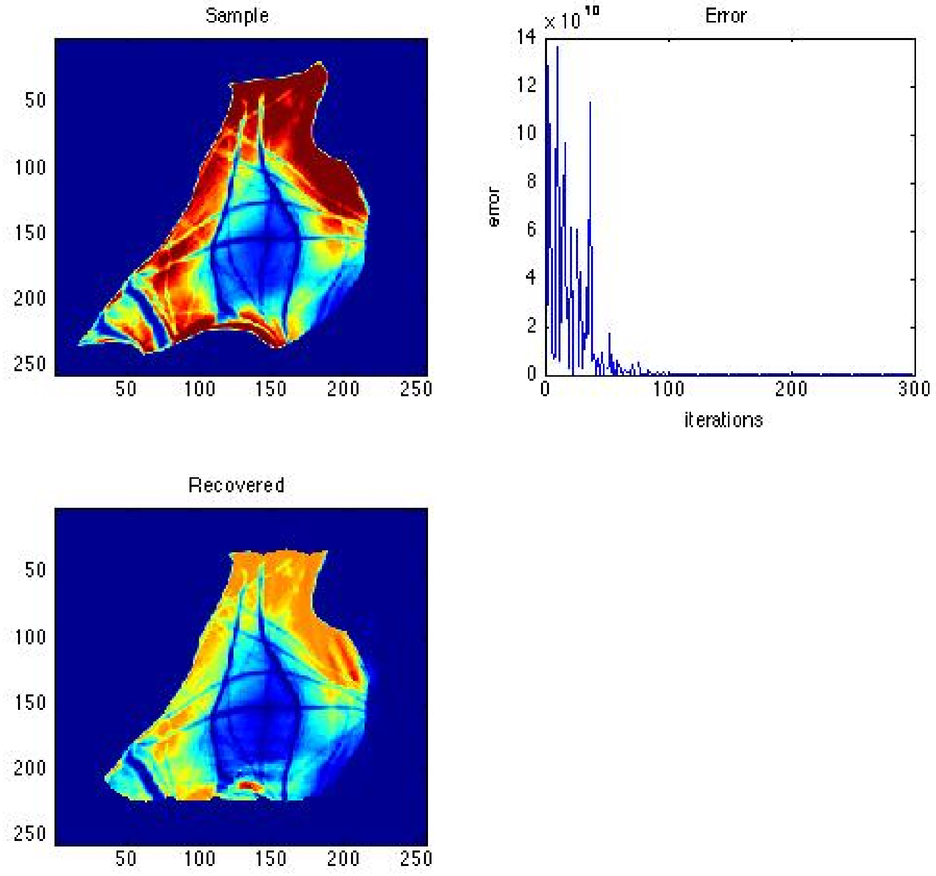

(b) Reconstructed image using Ptychography

Figure 2.11: Reconstructed images of the spine of the sea urchin showing voids for the organic matrix.

all visible, and the image looks closest to the sample. Again, to converge onto this solution took 100 iterations as shown in the error, which is 4 full loops of the probe positions.

Although many simulations were run in the project, many of them were used to fine tune the code, and to help find problems with the algorithms. The simulations presented in this section show the improvements in resolution of ptychography over conventional phase retrieval algorithms.

2.6 Experiment

As described, lensless x-ray diffraction requires coherent x-ray sources. One of these sources is located at the Rutherford Appleton Laboratories in Didcot, Oxfordshire. The source is a synchrotron called Diamond.

The experiment that was performed at diamond was not for use with ptychography, but could be used with ERHIO. The sample that you can see being loaded onto a slide in figure 2.12a is synthetic powder calcite. This was the control calcite sample for the experiment and a frame if the diffraction pattern that was recorded by the detector is shown in 2.12d.

The actual experiment was done in 3D, where the third angle was replicated by rocking the sample back and forth, and using time to replicate the z-direction in the experiment. The principle investigator for the project, Jesse Clarke (jesse.clarke@ucl.ac.uk) has developed some Matlab code that reconstructs the sample using the diffraction pattern obtained at the detector. The results of this reconstruction is shown in figure 2.12e. You can clearly see the rhombus shape of the calcite crystal. Although this is not as clear as it could be, you can see the main features.

This was then compared to the diffraction pattern obtained by a cube with remarkable similarity. The reason for the slight rotation, and the progression of the diffraction pattern was due to the fact the it was a rhombus shape, and that the z-direction was a tilt.

If this experiment had been using ptychography, we would have been able to see significantly more detail. The experiment used actual powered sea urchin test samples, however the results from these have not been obtained yet.

To perform ptychography experimentally, the setup would be similar to the one shown in the figures, however to create the overlap, we would have to move our sample in a plane perpendicular to the x-ray beam in a precise fashion. One of the lessons learnt from the simulation was to make sure that the uniqueness problem doesn't arise. This could be done by having a less periodic distance between the different probe positions. The different distances between the probes would ensure that each diffraction pattern would be distinguishable from the next.

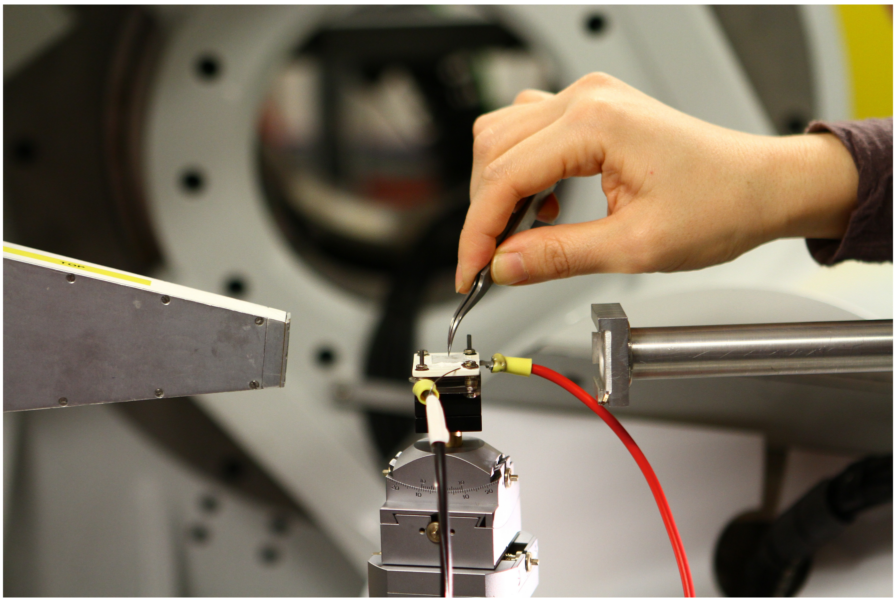

(a) Synthetic calcite sample being loaded

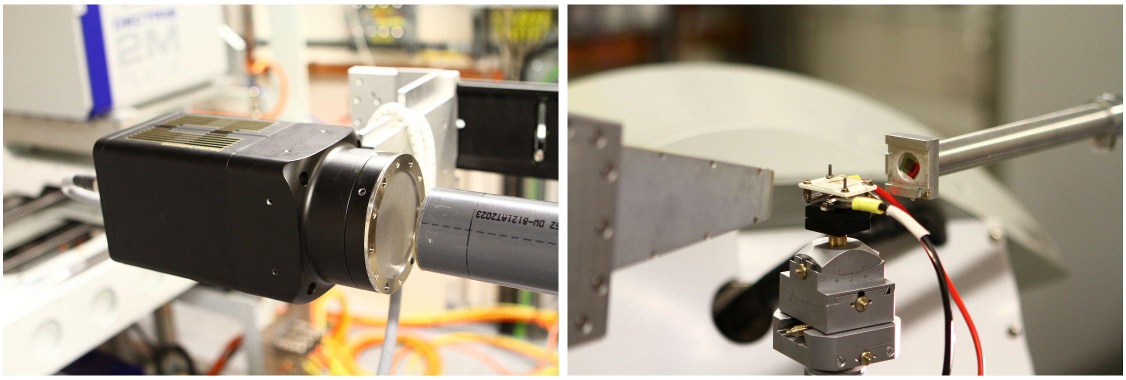

(b) Princeton electronics detector

(c) Another view of the sample and incoming x-ray direction

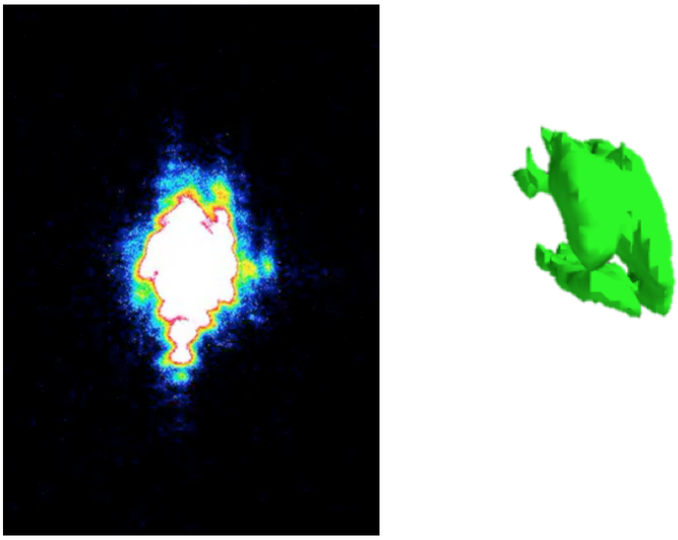

(d) Frame from the detector

(e) ERHIO reconstructed image

Figure 2.12: Photographs from Diamond and results

Chapter 3

Conclusion

In the first part of this report, biomineralisation was discussed, specifically with respect to the sea urchin. The test of the sea urchin is a remarkable substance, as are all of its skeletal elements. It is an extremely complicated object that we have not fully understood yet, and have yet to learn many lessons from it. The skeletal hard parts of the sea urchin are made from magnesium high calcite, however it differs from synthetic calcite in many different ways.

The test of the sea urchin has three main properties, each was explored. There are its lightweight, its resistance to stress, and its strength. The test was then explored at three different levels to understand why it is so different from regular calcite. The first level showed us that its dome like structure, along with its five fold symmetry gave it much strength. The individual large plates, and the smaller layers of plates were found to be joined together with collagen fibres. This gave it flexibility, and allow it to endure higher levels of strain.

The next level that was explored was at the micro level. This showed us that the calcite was not smooth and not made out of large continuos chunks, which was surprising as under polarised light, and x-ray diffraction the calcite appeared to be a single crystal. The calcite was indeed found to employ a fenestrated spongy like structure, where the empty space, or pores accounted for half of the volume of the structure. Under a microscope, it was hard to see the planar faces expected when viewing a crystal. The fenestrated structure also helped explain the lightweight property of the calcite along with its resistance to stress. Any cracks that would appear would not be allowed to propagate further than a few tens of microns, before the fenestrated structure stopped it. This is one of the possible reasons for the high strength, resistance to stress, and lightweight of calcite.

The final level that calcite was explored was at the nanoscale. Here it was shown that there must exist an organic matrix within the crystals of calcite. This was shown to have sparked controversy between scientists regarding crystallography of the calcite. If we think of this organic matrix within the calcite structure to be analogous to a brick and mortar substance where the bricks are the chunks of calcite and the mortar is the organic matrix, we can see how some people refuse to believe that the calcite is indeed a single crystal, but is in fact millions of domains of crystal that are all orientated in the same direction, so that they appear to be a single crystal. This clearly would be very difficult to prove, especially using x-ray diffraction as it shows how the calcite appears to be a single crystal.

After having explored biomineralisation, and the importance of the sea urchin test, the second part of the report moved onto a more mathematical discussion of x-ray diffraction, starting with the Bragg condition, and its equivalence to Laue, and how this allowed us to probe a crystal using x-rays.

We then looked at how diffraction patterns could be modelled on a computer simulation employing a version of the discrete Fourier transform called the fast Fourier transform found in Matlab. Once the simple modelling case had been set up, we then saw that by using lensless x-rays, we were loosing all the phase information, (that would have been retained by an objective lens) resulting in what is called the phase problem. Coherent diffraction imaging is thus concerned the the retrieval of the complex phase information that is lost in a coherent diffraction experiment. The main reason for not using lens's was to increase the resolution that could be probed.

The phase retrieval techniques used in this report were error reduction and hybrid input output, according to Fienup and ptychography according to Rodenburg. These algorithms were then mathematically discussed, and simulated, with ptychography showing clear advantages over the other algorithms.

We then looking at simulating calcite diffraction experiments using a complex sample. The first sample that was discussed was periodic and showed problems with both algorithms, however ptychography still had the clear advantage. The second sample was a TEM of the spine of a sea urchin, showing voids that were about 90nm in diameter. The ptychography algorithm managed to reproduce these effectively showing all the detail, while the ERHIO method was not as clear.

We clearly saw that ERHIO requires more stringent control over its variables than when compared with ptychography, especially the size of the guess. We have found that as long as the guess is the same size, or very close to the sample, then there is a high change that the algorithm would converge on the correct solution. Most of the time however, the algorithm would find another local solution, and converge upon that, giving a low error, but an incorrect solution.

The main problem that was found with ptychography was that the overlap parameter needed to be tweaked depending on the type of sample that was being reconstructed. We saw that for a periodic sample, if the different diffraction patterns were indistinguishable, then a solution would not be found. It is also necessary to have a large enough crystal that can be oversampled as to not have any aliasing issues.

Another factor that has not yet been discussed is the computational power required to compute the algorithms. An i5 quad core iMac running at 2.8ghz with 12gb of ram was used initially. This was found to be quite slow at running the algorithms, however when switching to an equivalent computer running an i5 quad core at 4ghz, the speed was effectively halved. This is due to the way Matlab works on the two operating systems. One method of reducing the time of the time taken for the computation of the algorithms would be to use c++ or other faster native coding applications. This was explored for this project, but was found to be too time consuming, and out of the scope for the project. Apart from that, optimising code was the next best solution to minimising the amount of computation time required. For reference, 1000 iterations of ERHIO would take up to 1min on the iMac, while taking 15seconds on the windows machine.

The ERHIO algorithms can easily be extended to work in 3D, as shown in the reconstruction in 2.12e, however this is not so easy with ptychography. One potential method would be to perform the ptychography on slices of 2d, then put them together, however this would be extremely laborious. Other methods that have been explored are to use an MRI type setup, where the sample is spun and a 3D diffraction pattern then made. These could potential extensions to this project, and would be very beneficial to the study of biominerals. The advantage of using hard x-rays are their penetration abilities, so it is feasible to perform ptychography in 3D. This would require some mapping of the code to be performed. Viewing 3D images was accomplished in another program called Mayavi which was used for the 3d visualisation used in 2.12e. Jesse Clarke used a mixture of Matlab and python code to create the data needed for these files.

Finally, we can conclusively say that imaging using coherent x-rays to probe biominerals at the nanoscale is one of the best methods to use to accomplish this. TEM only has a very shallow skin depth, even though it has superior resolution, but the advantage of using hard x-rays that go through the sample have already been discussed. The problem with coherent diffraction comes when using iterative algorithms to reconstruct the lost phase information. The most effective, and reliable method to do this would be to employ ptychography algorithms. There is massive scope for improvement of this algorithm, specifically so that it can be used in 3D. However for the purposes of biominerals, and biomineralised calcite, ptychography has the strength, and resolution to probe into regions that have not been probed before, and thus further our understanding of the complex process of biomineralisation, and the lessons we can learn from it.

Acknowledgements

I would like to thank Professor Ian Robinson for this project opportunity, and for his guidance throughout it. I would also like to thank Dr Jesse Clarke, whose help was integral in getting the Matlab code to run.

Bibliography

M. Abou and J. R. Stone. Classifying echinoid skeleton models : testing ideas about growth and form and form. *Society*, 37(4):686–695, 2011.

A. Arbor and M. Engineering. ULTRASTRUCTURAL AND MICROANALYTICAL RESULTS FROM ECHINODERM CALCITE : IMPLICATIONS FOR BIOMINERALIZATION. *Micron*, 15(2):85–90, 1984.

T. Bates. Uniqueness of Solutions to Two-Dimensional Fourier Phase Problems for Localized and Positive Images. *Image (Rochester, N.Y.)*, pages 205–217, 1984.

G. Donnay and D. L. Pawson. X-ray Diffraction Studies of Echinoderm Plates. *American Association for the Advancement of Science*, 166(3909):1147–1150, 2012.

J. R. Fienup. Reconstruction of an object from the modulus. *Optics Letters*, 3(1):27–29, 1978.

Y. D. Jean-Pierre Cuif and J. E. Sorauf. *Biominerals and Fossils Through Time.* Cambridge University Press, 2011.

K. M. W. Kenneth Simkiss. *Biomineralization - Cell Biology and Mineral Deposition.* Academic Press, Inc., 1989.

L. Klein and J. D. Currey. Echinoid Skeleton : Absence of a Collagenous Matrix. *Advancement Of Science*, 169(3951):1209–1210, 1970.

A. M. Maiden and J. M. Rodenburg. An improved ptychographical phase retrieval algorithm for diffractive imaging. *Ultramicroscopy*, 109(10):1256–62, Sept. 2009. ISSN 1879-2723. doi: 10.1016/j.ultramic.2009.05.012. URL `http://www.ncbi.nlm.nih.gov/pubmed/19541420`.

K. Mann, A. J. Poustka, and M. Mann. The sea urchin (Strongylocentrotus purpuratus) test and spine proteomes. *Proteome science*, 6: 22, Jan. 2008. ISSN 1477-5956. doi: 10.1186/1477-5956-6-22. URL `http://www.pubmedcentral.nih.gov/articlerender.fcgi?artid=2527298&tool=pmcentrez&rendertype=abs`

S. Mann. *Biomineralization - Principles and Concepts in Bioinorganic Materials Chemistry.* Oxford University Press, 2001.

F. C. Meldrum and R. Seshadri. Porous gold structures through templating by echinoid skeletal plates. *Chemical Communications*, (1):29–30, 2000. ISSN 13597345. doi: 10.1039/a907074e. URL `http://xlink.rsc.org/?DOI=a907074e`.

H.-U. Nissen. Crystal Orientation and Plate Structure in Echinoid Skeletal Units. *Advancement Of Science*, 166(3909):1150–1152, 2012.

D. M. Raup. *The Endoskeleton*, chapter 16. John Wiley and Sons, 1966.

J. Rodenburg, a. Hurst, a. Cullis, B. Dobson, F. Pfeiffer, O. Bunk, C. David, K. Jefimovs, and I. Johnson. Hard-X-Ray Lensless Imaging of Extended Objects. *Physical Review Letters*, 98(3):1–4, Jan. 2007a. ISSN 0031-9007. doi: 10.1103/PhysRevLett.98.034801. URL `http://link.aps.org/doi/10.1103/PhysRevLett.98.034801`.

J. M. Rodenburg, a. C. Hurst, and a. G. Cullis. Transmission microscopy without lenses for objects of unlimited size. *Ultramicroscopy*, 107(2-3):227–31, 2007b. ISSN 0304-3991. doi: 10.1016/j.ultramic.2006.07.007. URL `http://www.ncbi.nlm.nih.gov/pubmed/16959428`.

M. Stephen. Materials that naturally assemble themselves. *Chemical communications (Cambridge, England)*, (1):1–4, Jan. 2004. ISSN 1359-7345. doi: 10.1039/b310010n. URL `http://www.ncbi.nlm.nih.gov/pubmed/14737307`.

R. J. W. Stephen Mann, John Webb. *Biomineralization - Chemical and Biochemical Perspectives.* VCH-Germany, 1989.

X. Su, S. Kamat, and A. H. Heuer. The structure of sea urchin spines , large biogenic. *Materials Science*, 5:5545–5551, 2000.

M. Telford. Domes, arches and urchins: The skeletal architecture of echinoids (Echinodermata). *Zoomorphology*, 105(2):114–124, 1985. ISSN 0720213X. doi: 10.1007/BF00312146. URL `http://www.springerlink.com/content/x107tj7nhh329708/`.

K. M. Towe. Echinoderm Calcite : Single Crystal or Polycrystalline Aggregate. *Advancement Of Science*, 157(3792):1048–1050, 2012.

S. J. Tsrpunsry and P. R. Busncr. Structure of magnesian calcite from sea urchins. *Structure*, 78(1990):775–781, 1993.

J. Weber, R. Greer, B. Voight, E. White, and R. Roy. Unusual strength properties of echinoderm calcite related to structure. *Journal of ultrastructure research*, 26(5):355–66, Mar. 1969. ISSN 0022-5320. URL `http://www.ncbi.nlm.nih.gov/pubmed/5776310`.

S. Weiner. Organization of extracellularly mineralized tissues: a comparative study of biological crystal growth. *CRC critical reviews in biochemistry*, 20(4):365–408, Jan. 1986. ISSN 0045-6411. URL `http://www.ncbi.nlm.nih.gov/pubmed/3524990`.

Appendix A

Appendix Chapter 1

A.1 Complete diagrams of stereom fabrics. Smith (1980).

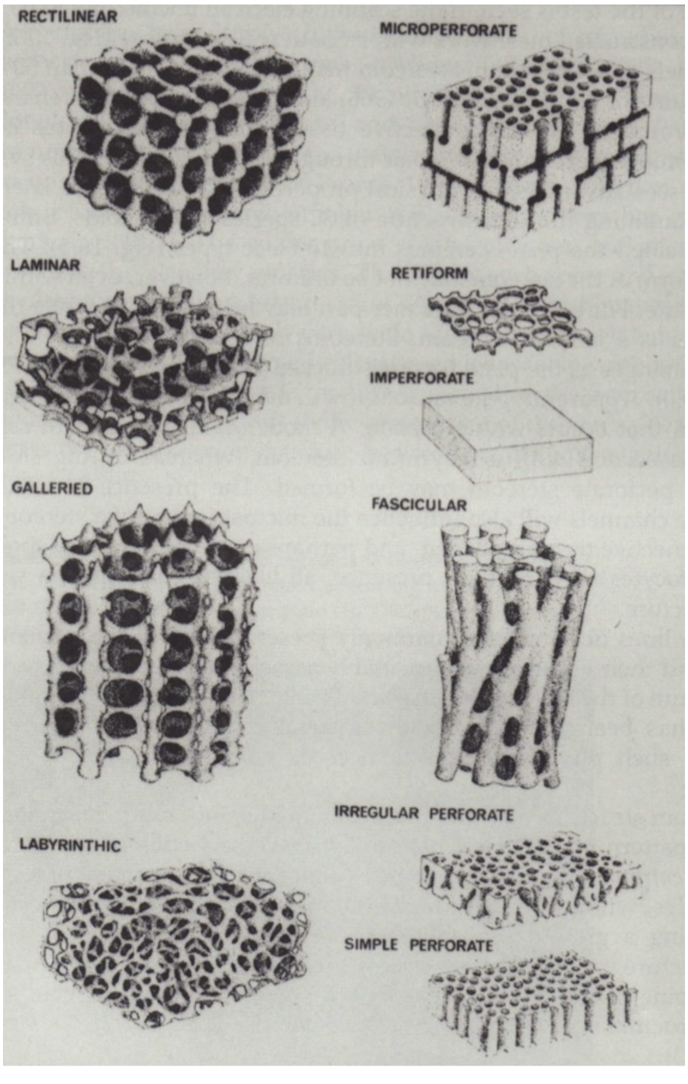

Appendix B

Appendix Chapter 2

B.1 Code for Sinc function

```
%This function creates a heaviside rectagular step function, and plots the %resulting
sinc function.
%by Gurvinder Chana, UCL Physics 2012
clear all
%This creates the step function
y=zeros(1,200);
y(1,98:102)=1;
%this defines the x-axis
dx=2/size(y,2);
x=-1+dx:dx:1;
%this does the fft
z=abs(fftshift(fft(fftshift(y))));
%fftshift is required to 'reorder' the fft
%always use fftshift(fft(ifftshift plot(x,z)
```

B.2 Function for Error Reduction

```
%Error reduction code by Gurvinder Chana
function [ gg ] = ER( f,g,t )
%ER Error reduction phase retrieval
% usage ER(measured,half estimate size,iteration)
s=length(f);
% this part is for size of estimate gg=zeros(s,s);
gg(s/2-g:s/2+g,s/2-g:s/2+g)=1;
```

```
%define support support=gg;
cnt=100;
for qq=1:t
%to monitor, and for videos
cnt=cnt+1;
scnt= num2str(cnt);
fg=fftshift(fftn(fftshift(gg)));
%fgr=complex(real(f),imag(fg));
phase=atan2(imag(fg),real(fg));
%get the current phase estimate
fgr=f.*exp(i.*phase);
%use 'measured' amplitude/modulus
%fgr=f.*(fg/abs(fg));
%need to check for zeros in 1/abs(fg)
ggr=fftshift(ifftn(fftshift(fgr)));
u=figure(1);
u=imagesc(abs(ggr));
saveas(u,scnt,'jpg');
close all
%apply
support gg=ggr.*support;
end
%apply 'reality constraint'
gg=real(gg);
end
```

B.3 Function for Hybrid Input Output

```
function [ gg ] = HIO( f,g,t )
%HIO Error reduction phase retrieval
% usage ER(measured,half estimate size,iteration)
s=length(f);
%size of estimate
gg=zeros(s,s);
gg(s/2-g:s/2+g,s/2-g:s/2+g)=1;
%define support
support=gg;
```

```
b=0.9
cnt=100;
for qq=1:t
cnt=cnt+1;
scnt= num2str(cnt);
fg=fftshift(fftn(fftshift(gg)));
%fgr=complex(real(f),imag(fg));
phase=atan2(imag(fg),real(fg));
%get the current phase estimate
fgr=f.*exp(i.*phase);
%use 'measured' amplitude/modulus
%fgr=f.*(fg/abs(fg));
%need to check for zeros in 1/abs(fg)
ggr=fftshift(ifftn(fftshift(fgr)));
u=figure(1);
u=imagesc(abs(ggr));
saveas(u,scnt,'jpg');
%apply support
gg=ggr.*support+((1-support).*(gg-b.*ggr));
end
%apply 'reality constraint'
gg=real(gg);
end
```

B.4 Top hat function for circular probe

```
function [ Circ ] = probe( R )
%PROBE tophat
n = 256;
Circ= zeros(n);
I = 1:n;
x = I-n/2;
y = n/2-I;
[X,Y] = meshgrid(x,y);
A = ((X).^2 + (Y).^2 <= R^2);
Circ(A) = 1;
end
```

B.5 Ptychography code

```
% Gurvinder Chana g.chana@ucl.ac.uk

% This is Ptychography code version 2

clear all

n=256; delta=1e-6; beta=1;

iterations=12;

array=zeros(n,n);

array_blank=array;

%initial Guess

%{

array(n/2-100:n/2+100,n/2-100:n/2+100)=1;

img2=subplot(2,1,2);

img2=imagesc(array);

img2=title('Guess');

%}

%sample

%[sample]=perforate;

sample=double(imread('final.jpg'));

img1=subplot(2,2,1);

img1=imagesc(sample);

img1=title('Sample');

%probe & positions

ill=probe(32);

%overlapping parameter setting.

%This section below created the probe positions.  The probe radius is given

%above in probe(x).  If you set p=x then the probes will not overlap.

p=32;

pp=2.*p;

posx=[pp,pp,pp,pp,pp, p,p,p,p,p ,0,0,0,0,0, -p,-p,-p,-p,-p, -pp,-pp,-pp,-pp,-pp];

posy=[pp,p,0,-p,-pp, pp,p,0,-p,-pp ,pp,p,0,-p,-pp ,pp,p,0,-p,-pp ,pp,p,0,-p,-pp];

nposn=numel(posx);

data=[];

%generate the data

for qq=1:nposn

%figure(1)
```

```
%
imagesc(abs(sample.*circshift(ill,[posy(qq) posx(qq)]))) data(:,:,qq)=abs(fftshift(fftn(ifftshift
posx(qq)])))))).^2;
%figure(2)
%
imagesc(abs(data(:,:,qq)))
end
%now do the iterative procedure
obj=ones(size(sample));
cnt=500;
for qq=1:iterations
for ww=1:nposn
cnt=cnt+1;
scnt=num2str(cnt);
%shifted illumination
sill=circshift(ill,[posy(ww) posx(ww)]);
%create the wave for each position psi=P*O
psi=obj.*sill;
%propagate
psi_d=fftshift(fftn(ifftshift(psi)));
%replace modulud
psi_dm=sqrt(data(:,:,ww)).*exp(1i*angle(psi_d));
%calculate error
nume=abs(abs(psi_d).^2-abs(psi_dm).^2).^2;
error=sum(nume(:))/sum(abs(psi_dm(:)).^2);
%return to the sample plane
psi_s=fftshift(ifftn(ifftshift(psi_dm)));
%create update function
Ur=(abs(sill).*conj(sill))./(max(abs(sill(:))).*abs(sill).^2+delta);
%update object
obj=obj+beta*Ur.*(psi_s-psi);
img3=subplot(2,2,3);
img3=imagesc(abs(obj));
img3=title('Recovered');
err(cnt-500)=error;
```

```
img4=subplot(2,2,2);
img4=plot(err);
img4=title('Error');
img4=xlabel('iterations');
img4=ylabel('error');
%saveas(img3,scnt,'jpg');
end
end
```

B.6 ERHIO code

```
%Phasing ER and HIO
%By Gurvinder S Chana, g.chana@ucl.ac.uk
clear all
tic
%define array
s=256;
ss=zeros(s,s);
%make sample ss
%
n=40;
ss(s/2-n:s/2+n,s/2-n:s/2+n)=1;
ss(:,[150,149,151])=0;
samplemain=ss;
%
%{ [sp]=perforate;
samplemain=ss.*sp; %}
%jpg import
%{
ss1= imread('porousz.jpg');
samplemain=(double(ss1).*ss);
%}
%create measured
f=abs(fftshift(fftn(fftshift(samplemain))));
%defines number of iterations to do.  Hio first, then some Er, then HIO to
%finish.
itr1=200; %number of HIO first
```

```
itr2=50; %number of ER second
itr3=40; %number of HIO last
%define support
updsup=zeros(s,s);
g=75;
updsup(s/2-g:s/2+g,s/2-g:s/2+g)=1;
support=updsup; %size of support
b=0.9;
cnt=100;
%part 1 HIO
for qq=1:itr1
cnt=cnt+1;
scnt=num2str(cnt);
fg=fftshift(fftn(fftshift(updsup)));
%transform support
phase=atan2(imag(fg),real(fg));
%get the current phase estimate
fgr=f.*exp(i.*phase);
%use 'measured' amplitude/modulus
ggr=fftshift(ifftn(fftshift(fgr)));
%back to real space
updsup=ggr.*support+((1-support).*(updsup-0.9.*ggr));
%support
%error
nume=sum(abs((abs(fg).^2)-(abs(f).^2))).^2; error=nume/sum(abs(fg).^2);
err(cnt-100)=error;
%figures
%error
main=figure(1);
im1=subplot(2,2,4);
im1=title('Error');
im1=xlabel('Iterations');
im1=ylabel('Error');
im1=plot(err);
%sample
im2=subplot(2,2,1);
im2=title('Sample');
im2=imagesc(abs(samplemain));
```

```
%recovered
im3=subplot(2,2,2);
im3=imagesc(abs(ggr));
im3=title('hio');
%amplitude
im4=subplot(2,2,3);
im4=image(abs(fg));
%saveas(main,scnt,'jpg');
end
%Part 2 ER
for qqq=1:itr2
cnt=cnt+1;
scnt=num2str(cnt);
fg=fftshift(fftn(fftshift(updsup)));
phase=atan2(imag(fg),real(fg));
fgr=f.*exp(i.*phase);
ggr=fftshift(ifftn(fftshift(fgr)));
updsup=ggr.*support;
nume=sum(abs((abs(fg).^2)-(abs(f).^2))).^2;
error=nume/sum(abs(fg).^2);
err(cnt-100)=error;
%figures
%error
main=figure(1);
im1=subplot(2,2,4);
im1=title('Error');
im1=xlabel('Iterations');
im1=ylabel('Error');
im1=plot(err);
%sample
im2=subplot(2,2,1);
im2=title('Sample');
im2=imagesc(abs(samplemain));
%recovered
im3=subplot(2,2,2);
im3=imagesc(abs(ggr));
im3=title('er');
%amplitude
```

```
im4=subplot(2,2,3);
im4=image(abs(fg));
%saveas(main,scnt,'jpg');
end
%Part 3 HIO
for qqqq=1:itr3
cnt=cnt+1;
scnt=num2str(cnt);
fg=fftshift(fftn(fftshift(updsup)));
%transform support
phase=atan2(imag(fg),real(fg));
%get the current phase estimate
fgr=f.*exp(i.*phase);
%use 'measured' amplitude/modulus
ggr=fftshift(ifftn(fftshift(fgr)));
%back to real space
updsup=ggr.*support+((1-support).*(updsup-b.*ggr));
%support
%error nume=sum(abs((abs(fg).^2)-(abs(f).^2))).^2;
error=nume/sum(abs(fg).^2);
err(cnt-100)=error;
%figures
%error
main=figure(1);
im1=subplot(2,2,4);
im1=title('Error');
im1=xlabel('Iterations');
im1=ylabel('Error');
im1=plot(err);
%sample
im2=subplot(2,2,1);
im2=title('Sample');
im2=imagesc(abs(samplemain));
%recovered
im3=subplot(2,2,2);
im3=imagesc(abs(ggr));
im3=title('hio');
%amplitude
```

```
im4=subplot(2,2,3);
im4=image(abs(fg));
%saveas(main,scnt,'jpg');
end
toc
```